PHYSICAL REVIEW E **80**, 031123 (2009)

Topology, symmetry, phase transitions, and noncollinear spin structures

F. A. N. Santos and M. D. Coutinho-Filho
Laboratório de Física Teórica e Computacional, Departamento de Física, Universidade Federal de Pernambuco,
50670-901 Recife, PE, Brazil

(Received 7 January 2009; published 17 September 2009; publisher error corrected 30 September 2009)

We use a topological approach to describe the frustration- and field-induced phase transitions exhibited by the infinite-range *XY* model on the AB_2 chain, including noncollinear spin structures. For this purpose, we have computed the Morse number and the Euler characteristic, as well as other topological invariants, which are found to behave similarly as a function of the energy level in the context of Morse theory. In particular, we use a method based on an analogy with statistical mechanics to compute the Euler characteristic, which proves to be quite feasible. We also introduce topological energies which help us to clarify several properties of the transitions, both at zero and finite temperatures. In addition, we establish a nontrivial direct connection between the thermodynamics of the systems, which have been solved exactly under the saddle-point approach, and the topology of their configuration space. This connection allows us to identify the nondegeneracy condition under which the divergence of the density of Jacobian's critical points $[j_l(E)]$ at the critical energy of a topology-induced phase transition, proposed by Kastner and Schnetz [Phys. Rev. Lett. **100**, 160601 (2008)] as a necessary criterion, is suppressed. Finally, our findings and those available in the literature suggest that the cusplike singularity exhibited both by the Euler characteristic and the topological contribution for the entropy at the critical energy, put together with the divergence of $j_l(E)$, and emerge as necessary and *sufficient* conditions for the occurrence of the finite-temperature topology-induced phase transitions examined in this work. The general character of this proposal should be subject to a more rigorous scrutiny.

DOI: 10.1103/PhysRevE.80.031123 PACS number(s): 75.10.Hk, 05.20.−y, 05.70.Fh

I. INTRODUCTION

Recently, methods and concepts of geometry and differential topology, especially those from Morse theory, have been used to propose a topological approach to phase transitions (PTs) [1]. In fact, based on the temperature- or energy-dependent singular behavior presented by some geometrical observables at the critical point, it has been conjectured [2] that the occurrence of thermodynamic PTs is connected to a nontrivial change in the topology of the configuration space. Later, it has been proved that this conjecture is a necessary condition to phase transitions in systems described by smooth, finite-range, and confining microscopic interaction potentials [3]. However, the necessity theorems do not exclude the possibility that infinite-range [mean-field-like (MF-like)] or long-range models exhibit PTs that are connected to a topological change in configuration space [1]. Very recently, following some of the arguments used to prove the above theorems, a necessity criterion for topology-induced PT was proved [4], namely, the divergence of the density of Jacobian's critical points at the critical energy level in the thermodynamic limit. This criterion introduced a geometrical aspect associated to microscopic properties, i.e., curvatures at the saddle points of the potential, confirmed the topological origin of the phase transitions in two exactly infinite-range solvable models, the infinite-range *XY* model [5,6] and the *k*-trigonometrical model [7], and excluded that occurring in the spherical model with nearest-neighbor interaction [8]. In fact, as pointed out by Pettini [9], this model is not a counterexample for the necessity theorems [3] since the spherical constraint introduces long-range interaction. The above ideas have also proved useful in the description of PT in models of DNA denaturation [10] and of protein folding [11].

The physical motivation of our work is to present a topological characterization of the zero- and finite-temperature PTs exhibited by two *XY* models on the AB_2 chain [see Fig. 1(a)] at the MF level: the frustrated AB_2-*XY* model and the AB_2-*XY* model in the presence of a magnetic field. No kinetic energy effects are considered. The AB_2 chain has a special unit cell topology that enriches the variety of spin phases, including noncollinear structures, and is of theoretical and experimental relevance in the context of low-dimensional strongly correlated systems [12]. In fact, the physical properties of the quasi-one-dimensional magnetic compound azurite are successfully explained by the frustrated AB_2 (or distorted diamond) chain [13]. In Fig. 1(b) we also display a chain with a distinct three-site unit cell topology [14]. Without interaction between spins at *B* sites, this chain is associated with the organic compound Poly(1,4-bis(2, 2, 6, 6-tetramethyl-4-piperidyl-1-oxyl)-butadiene)

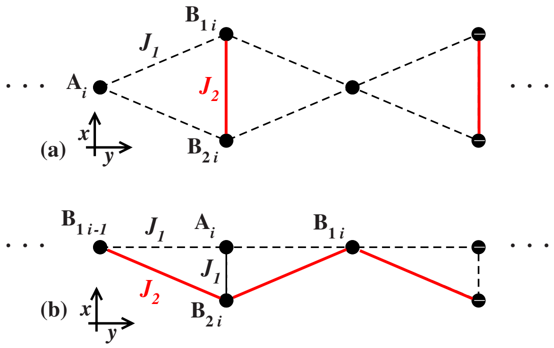

FIG. 1. (Color online) Frustrated AB_2 chain: only first-neighbor competing *AF* couplings, J_1 and J_2, are indicated. (b) Distinct chain with three-site unit cell topology (see text).

(poly-BIPO), which is made of polyacetylene-based radicals with an unpaired electron per unit cell [15]. On the other hand, for Hamiltonian with first-neighbor spin interactions only, the AB_2 chain shown in Fig. 1(a) exhibits local invariance under the exchange of B sites at the same unit cell, a symmetry which is not shared by the chain in Fig. 1(b); notice also that the coordination numbers of some sites in these chains are distinct. Within the standard MF approximation, the molecular field on a site depends on its coordination number, which thus enhances the magnitude of the exchange field in the MF self-consistent equations. However, for infinite-range interactions, both chains have $3N_c^2$ pairs of spin at sites A-B_1, A-B_2, and B_1-B_2 bonded by exchange interactions (see Fig. 1); in this framework both chains are thus equivalent and the dimensionality of the system and the actual positions of the spins are immaterial. Moreover, under these circumstances, both chains share an invariance under the exchange of any pair of B sites. In any case, it is well known that the MF approximation for the short-range model can be made identical to the exact solution of the corresponding model with infinite-range interactions as long as the values of the effective exchange constants of the latter model are balanced in such a way that the coordination number effect is properly considered [16], as shown below.

From now on we focus on the bipartite AB_2-XY chain with three sites (named A, B_1, and B_2) per unit cell and two antiferromagnetic competing couplings, J_1 ($\equiv 1$) and J_2 ($\equiv J$), as illustrated in Fig. 1(a), which we model through the infinite-range classical planar AB_2-XY Hamiltonian with effective coupling values chosen to match the self-consistent conditions of the standard MF approximation [17,18],

$$H = \sum_{i,j=1}^{N_c} \frac{1}{N_c}\{z_{AB}\mathbf{S}_{A_i}\cdot(\mathbf{S}_{B_{1j}}+\mathbf{S}_{B_{2j}}) + z_B J\mathbf{S}_{B_{1i}}\cdot\mathbf{S}_{B_{2j}} - \mathbf{h}\cdot(\mathbf{S}_{A_i}+\mathbf{S}_{B_{1i}}+\mathbf{S}_{B_{2i}})\}, \tag{1}$$

where H measures the total energy of the system for a given microscopic spin configuration (see below), N_c is the total number of unit cells, $z_{AB}=2$ and $z_B=1$ are the coordination numbers of sites A (first-neighbor J_1 couplings) and B (first-neighbor J_2 couplings), $\mathbf{S}_{\mathbf{A}1}$, $\mathbf{S}_{\mathbf{B}1i}$, and $\mathbf{S}_{\mathbf{B}2i}$ are classical spin variables with unit size, and $\mathbf{h}$ is the magnetic field along the x direction [see Fig. 1(a)]. The results for any other system with three spins per unit cell are completely equivalent and easily obtained by adjusting the corresponding coordination numbers.

The paper is organized as follows: in Sec. II we discuss the topology of configuration space in light of fundamental properties of Morse theory and topological invariants, such as the Euler characteristic and the density of Jacobian's critical points. Further, we present an alternative method to compute topological invariants. In Sec. III, we apply these methods to study both the zero- and finite-temperature PTs exhibited by the infinite-range AB_2-XY models in the presence of frustration or magnetic field. The thermodynamics of the models are exactly derived under the saddle-point approach. In this section, we also revisit the standard infinite-range XY model in the presence of a field. Finally, In Sec. IV we present some concluding remarks, and in Appendixes A and B we report on symmetry properties of the models and results of additional topological invariants, such as the Morse number as well as the topological contribution to the entropy, respectively.

II. TOPOLOGY OF CONFIGURATION SPACE

We first introduce the magnetization given by

$$\mathbf{m}_\alpha \equiv \frac{\mathbf{S}_\alpha}{N_c} = (m_{\alpha x}, m_{\alpha y}) = \left(\frac{1}{N_c}\sum_{i=1}^{N_c} \cos\,\theta_{\alpha i}, \frac{1}{N_c}\sum_{i=1}^{N_c} \sin\,\theta_{\alpha i}\right), \tag{2}$$

where $\alpha = A$, B_1, or B_2 and $\theta_{\alpha i}$ refers to the angles of $\mathbf{S}_{\alpha i}$ with respect to the local x-y coordinate axis at site α_i. Further, we use the symmetry conditions to restrict our analysis to A and B (B_1 or B_2) sites (see Appendix A). We are primarily concerned with finding the critical points of the Morse function [19], $\mathcal{H}=H/N_c$, i.e., the energy per unit cell for a given microscopic spin configuration through the equations

$$\frac{\partial\mathcal{H}(\theta_A,\theta_B)}{\partial\theta_{\alpha i}} = 0, \quad i=1,\ldots,N_c, \quad \alpha = A,B \tag{3}$$

in the manifold M defined by the $2N_c$-dimensional configuration space. Since Morse functions on M are dense on the space of smooth functions on M, if $\mathcal{H}$ is not a proper Morse function, we can transform it onto a Morse function by adding an arbitrarily small perturbation [1,20]. Thus, we restrict our analysis to the isolated critical points of $\mathcal{H}$. Our goal is to compute the Euler characteristic $\chi(M_E)$ of the submanifolds M_E, with $\mathcal{H}$ not greater than a given value of energy per unit cell E,

$$\chi(M_E) = \sum_{k=0}^{2N_c}(-1)^k\mu_k(M_E), \tag{4}$$

where the Morse number μ_k is the number of critical points of M_E with k as negative eigenvalues of the Hessian (see Appendix B),

$$\mathcal{H}_{ij} = \frac{\partial^2\mathcal{H}(\theta_A,\theta_B)}{\partial\theta_{\alpha i}\,\partial\theta_{\alpha j}}, \quad i,j=1,\ldots,N_c, \quad \alpha=A,B, \tag{5}$$

i.e., with index k [5,6]. In our analysis, it will prove useful to define the minimum (maximum) topological energy, $E_{T\min}$ ($E_{T\max}$), below (above) which the topological invariants are zero (or display no variation). We emphasize that $\chi(M_E)$ is zero for $E<E_{T\min}$ and $E>E_{T\max}$; nontrivial values occur only for $E_{T\min}\leq E\leq E_{T\max}$, as shown in the examples presented in Sec. III. Moreover, in order to measure the (nonanalytic) saddle-point contributions from the critical points in the neighborhood of E to the entropy [4], we also compute the density of Jacobian's critical points in the thermodynamic limit, given by

$$j_l(E) = \lim_{N_c \to \infty} \frac{1}{2N_c} \ln\left(\sum_{q_c \in Q_l(E,E+\delta E)} J(q_c) / \sum_{q_c \in Q_l(E,E+\delta E)} 1 \right), \tag{6}$$

where $J(q_c)$ is the Jacobian determinant and $Q_l(E,E+\delta E)$ denotes the set of critical points q_c with index $k(q_c)=l$ (mod 4) and with critical values $\mathcal{H}(q_c)$ in the interval $[E,E+\delta E]$ [4].

In order to turn the computation of $\chi(M_E)$ more feasible, we use an analogy with statistical mechanics in the context of the microcanonical ensemble. Let $\Gamma_\chi(E)$ denotes the difference between the Euler characteristics in the even-dimensional compact submanifolds [21] $M_{E+\delta E}$ and M_E,

$$\Gamma_\chi(E) \equiv \chi(M_{E+\delta E}) - \chi(M_E), \tag{7}$$

where $\Delta\varepsilon \ll \delta E \ll \Delta E$; here ΔE is the interval of energy in which $\chi(M_E)$ is nonzero and $\Delta\varepsilon$ is the average distance between two neighbor critical levels. Then,

$$\Gamma_\chi(E) \approx \omega_\chi(E)\delta E, \tag{8}$$

where $\omega_\chi(E)$ is the density of critical points of $\mathcal{H}$ at energy E, with weight $(-1)^k$. Since for systems in which the number of isolated critical points increases as 2^{N_c} (see below), $|\chi(M_E)|$ grows exponentially with N_c, the following definitions are equivalent in the thermodynamic limit [up to $\mathcal{O}(\ln 2N_c)$]:

$$\ln|\chi(M_E)| = \ln|\Gamma_\chi(M_E)| = \ln|\omega_\chi(M_E)|. \tag{9}$$

Further, for sufficiently large N_c, we can take

$$\ln|\omega_\chi(M_E)| \approx \ln \omega_c(E), \tag{10}$$

where $\omega_c(E)$ is the microcanonical density of critical points. For example, for the models studied in this work, we find that $\Delta\varepsilon \sim (\Delta E/N_c^2)$ and $\Delta E \sim 10$; so, we have computed $\chi(M_E)$ using $\delta E \sim (\Delta E/N_c)$ and $N_c=10^3$. With these prescriptions, we have verified Eqs. (9) and (10) to very good numerical accuracy.

III. TOPOLOGY AND NONCOLLINEAR SPIN STRUCTURES

A. Frustrated *AB*$_2$-*XY* model

In the frustrated AB_2-XY model ($J\neq 0$, $h=0$), the symmetry condition implies $m_{B_1y}=-m_{B_2y}\equiv m_{By}$ and $m_{B_1x}=m_{B_2x}\equiv m_{Bx}$ (see Appendix A). In fact, this solution turns out to be the appropriate one under the physical constraint of zero transversal magnetization. The Hamiltonian per unit cell in terms of collective variables thus reads

$$\mathcal{H}(\theta_A,\theta_B) = 4m_{Ax}m_{Bx} + J(m_{Bx}^2 - m_{By}^2). \tag{11}$$

The exact solution of the model at $T\neq 0$ results from computing the canonical partition function

$$Z(\beta \equiv 1/T, N_c) = \int \prod_{i=1}^{N_c} d\theta_{Ai} d\theta_{Bi} \exp[-\beta N_c \mathcal{H}(\theta_A,\theta_B)], \tag{12}$$

with

$$\mathcal{H}(\theta_A,\theta_B) = (m_{Ax}/\sqrt{J} + \sqrt{J}m_{Bx})^2 - Jm_{By}^2 - m_{Ax}^2/J, \tag{13}$$

although, for $0<J\leq 1$, the quadrature $\mathcal{H}=2[(m_{Ax}+m_{Bx})^2 - 2m_{Ax}^2 - (2-J)m_{Bx}^2 - Jm_{By}^2]$ is more suitable for numerical computation. Using the identities

$$\exp(-cy_i^2) = \frac{1}{\sqrt{\pi}} \int_{-\infty}^{+\infty} \exp(-x_i^2 + 2i\sqrt{c}x_i y_i) dx_i, \tag{14}$$

with $y_1=m_{Ax}/\sqrt{J}+\sqrt{J}m_{Bx}$, $y_2=m_{By}$, and $y_3=m_{Ax}$, and

$$I_0(\sqrt{x^2+y^2}) = \frac{1}{2\pi} \int_0^{2\pi} d\theta \exp(x\cos\theta + y\sin\theta), \tag{15}$$

where I_0 is the zero-order modified Bessel function, we obtain

$$Z(\beta,N_c) = \left(\frac{N_c}{4\pi\beta J}\right)^{3/2} \int_{-\infty}^{+\infty} \prod_{i=1}^{3} dz_i \times \exp\left[-N_c \left\{ \sum_{i=1}^{3} \frac{z_i^2}{4\beta J} - \ln 2\pi I_0\left[\frac{2}{J}(iz_1 - z_2)\right] - \ln 2\pi I_0(\sqrt{z_3^2 - z_1^2}) \right\} \right], \tag{16}$$

with $z_i = 2\sqrt{\beta J/N_c}x_i$, $i=1,2,3$.

Now, using the saddle-point method, the free energy reads

$$F(T;J) = -\lim_{N_c\to\infty} \frac{1}{\beta N_c} \ln Z(\beta,N_c) = \frac{1}{\beta}\left\{ \sum_{i=1}^{3} \frac{z_i^2}{4\beta J} - \ln 2\pi I_0\left[\frac{2}{J}(iz_1 - z_2)\right] - \ln 2\pi I_0(\sqrt{z_3^2 - z_1^2}) \right\}, \tag{17}$$

whose extremum solutions satisfy the set of self-consistency equations for the following: (i) for $z_3\neq 0$ and $2z_1+iz_2=0$,

$$\frac{\sqrt{z_3^2 - z_1^2}}{2\beta J} - \frac{I_1}{I_0}(\sqrt{z_3^2 - z_1^2}) = 0 \tag{18}$$

and

$$\frac{iz_1}{\beta J} + \frac{I_1}{I_0}\left(\frac{2}{J}(-iz_1)\right)\frac{2}{J} = 0; \tag{19}$$

(ii) for $z_3=0$,

$$\frac{iz_1 - z_2}{2\beta J} + \frac{I_1}{I_0}(iz_1) = 0 \tag{20}$$

and

$$\frac{z_2}{2\beta J} + \frac{I_1}{I_0}\left(\frac{2}{J}(iz_1 - z_2)\right)\frac{2}{J} = 0. \tag{21}$$

The associated zero-field magnetization is given by

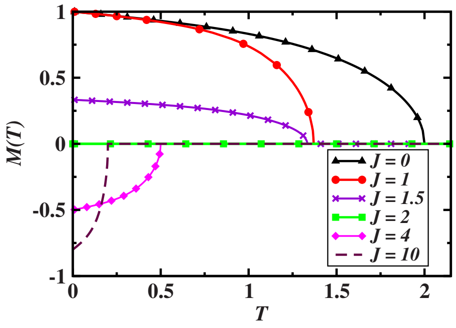

FIG. 2. (Color online) Frustrated AB_2-XY model. T-dependent magnetization for different values of J.

$$M(T;J) = -\lim_{h\to 0}\frac{1}{\beta}\frac{\partial F(\beta,h;J)}{\partial h}, \tag{22}$$

with addition of the Zeeman term, $-h(m_{Ax}+2m_{Bx})$, in Eq. (11). From the solution that minimizes the free energy we can compute $T_c(J)$, above which $M(T;J)=0$, and

$$E_c(T_c;J) = \frac{\partial[\beta F(\beta=\beta_c;J)]}{\partial\beta} = 0, \quad \forall \quad J. \tag{23}$$

The T-dependent magnetization is shown in Fig. 2. For $0 < J \leq 2$, $T_c(J)$ decreases with J, leading to zero magnetization at $J=2$. For $J>2$ the magnetization points in the opposite direction. These features suggest a frustration-induced phase transition at $T=0$. In fact, for $0\leq J<1$, simple minimization of $\mathcal{H}(\theta_A,\theta_B)$ in Eq. (11) gives a ferrimagnetic phase with energy

$$E_{\min}(J) = -4 + J, \quad 0 \leq J < 1, \tag{24}$$

in agreement with Lieb-Mattis theorem [22]. At $J=1$, the system undergoes a frustrated-induced second-order transition to a canted phase defined by

$$\cos(\theta_B) = \frac{1}{J} \tag{25}$$

and energy

$$E_{\min}(J) = -\frac{2}{J} - J, \quad J \geq 1. \tag{26}$$

In the following we will present a topological description of the PT exhibited by the system both at $T=0$ and at finite temperature. For this aim, we will examine the topology of configuration space in detail.

First we mention that the accessible configurations are defined by the cylinder

$$\mathcal{C}_{\mathcal{B}} = \{(m_{Ax},m_{Bx},m_{By}): -1 \leq m_{Ax} \leq 1, m_{Bx}^2 + m_{By}^2 \leq 1\}. \tag{27}$$

Therefore, the equipotential submanifolds of $\mathcal{H}(\theta_A,\theta_B)$ are obtained by diagonalization of its quadratic form under the constraint of $\mathcal{C}_B$ for a given energy E. Denoting by m_1 and m_2 the eigenvectors of the quadric, with eigenvalues λ_1 and λ_2, respectively, the Cartesian equation of the normalized surface reads

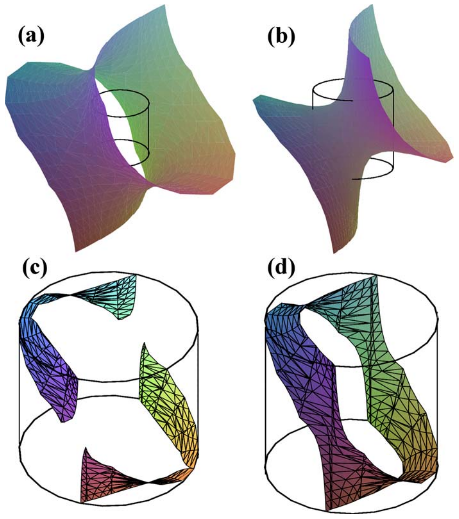

FIG. 3. (Color online) Intersection surfaces between equipotential submanifolds M_E and $\mathcal{C}_{\mathcal{B}}$. (a) For $E=-4$ and $J=1$, we have $E < E_{\min}(J=1)=-3$, so there is no intersection between M_E and $\mathcal{C}_{\mathcal{B}}$. (b) For $E=-2$ and $J=1$, we have $E>E_{\min}(J)$, so M_E is inside $\mathcal{C}_{\mathcal{B}}$, with nonzero topological invariants. (c) For $E=-2.1$ and $J=2$, despite nonempty intersection, the topological invariants are null. (d) For $E=-1.9$ and $J=2$, we have $E>E_{\mathcal{T}\min}$, so the intersection between M_E and $\mathcal{C}_{\mathcal{B}}$ is nonzero and isomorphous to the hyperboloid.

$$\frac{\lambda_1 m_1^2}{E} + \frac{\lambda_2 m_2^2}{E} - \frac{J m_{By}^2}{E} = 1. \tag{28}$$

We thus get, $\forall$ J, a hyperboloid of one sheet for $E<0$, a cone for $E=0$, and a hyperboloid of two sheets for $E>0$. In particular, at the highest symmetry point ($\theta=120°$), $J=2$ and $E_{\mathcal{T}\min}=-2$, with $M(T;J=2)=0$, we obtain the *golden hyperboloid*, a quadratic form whose coefficients are the golden number and its conjugate [23],

$$-\left(\frac{1+\sqrt{5}}{2}\right)m_1^2 - \left(\frac{1-\sqrt{5}}{2}\right)m_2^2 + m_{By}^2 = 1. \tag{29}$$

In approaching the critical energy $E_c(T;J)=0$, $\forall$ J, from below ($E<E_c$), we would like to mention some relevant features. For $E<E_{\min}(J)$ there is no intersection between the equipotential submanifolds M_E and $\mathcal{C}_{\mathcal{B}}$ [see Fig. 3(a) for $E=-4$ and $J=1$]. For $E=E_{\min}(J)$, M_E *touches* the cylinder $\mathcal{C}_{\mathcal{B}}$ (not shown in Fig. 3). For $E>E_{\min}(J)=E_{\mathcal{T}\min}(J)$ and $0\leq J \leq 1$, M_E is *inside* $\mathcal{C}_{\mathcal{B}}$, with nonzero topological invariants and isomorphous to the hyperboloid [see Fig. 3(b) for $E=-2$ and $J=1$]. However, the topological invariants become nonzero not necessarily at $E_{\min}(J)$ [see Fig. 3(c) for $E=-2.1$ and $J=2$]. In fact, the topological invariants become nonzero only when two disconnected regions of the intersection surface become connected at $E=E_{\mathcal{T}\min}(J)$. For $1<J<2$ and $E_{\min} \leq E < E_{\mathcal{T}\min}(J)$, the intersection is nonzero but the topological invariants vanish. For $J\geq 2$ and $E_{\mathcal{T}\min}(J) \leq E < E_c$ $(=0, \forall$ $J)$ the intersection is isomorphous to the hyperboloid, thus leading to a discontinuity in the topological invariants, as illustrated in Fig. 3(d) for $J=2$ and $E=-1.9$. On the other hand, for $E_c(T;J) < E \leq E_{\mathcal{T}\max}(J)=E_{\max}(J)$ the intersection surfaces are two-sheet hyperboloids.

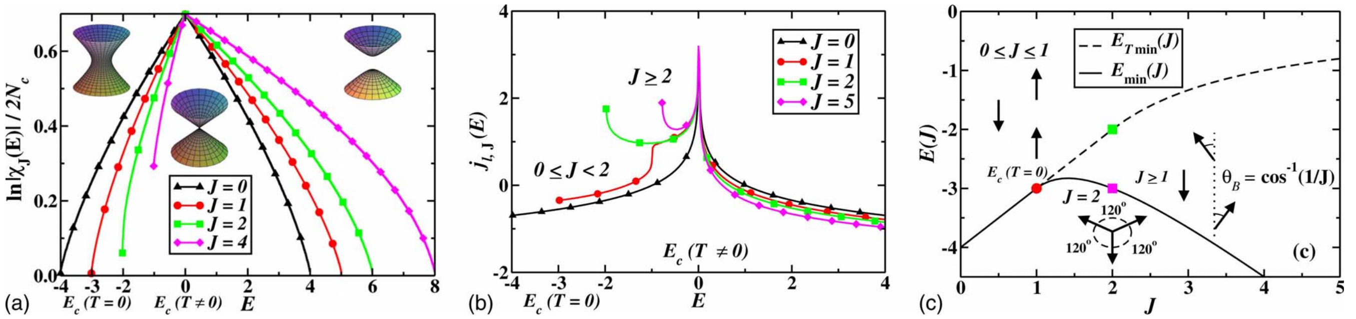

FIG. 4. (Color online) Frustrated AB_2-XY model. (a) Cusplike pattern exhibited by $\ln|\chi_J(E)|/2N_c$ measured on the surface defined by the intersection of the equipotential surface and the cylinder $\mathcal{C}_B$ (see text). For $E<0$, the equipotential surfaces are one-sheet hyperboloids; at $E_c(T\neq 0)=0\ \forall\ J$, we have a cone and for $E>0$ we have two-sheet hyperboloids. For $J\geq 2$, $\ln|\chi_J(E)|/2N_c$ is discontinuous at $E_{T\min}(E)$ due to intersection surfaces with zero $\chi_J(E)$ for $E_{\min}(J)\leq E<E_{T\min}(J)$. The intersection surfaces and $\ln|\chi_J(E)|/2N_c$ vanish at $E_{\max}=E_{T\max}=4+J$. (b) Divergence of $j_{l,J}(E)$ at $E_c(T\neq 0)=0\ \forall\ J$. The golden hyperboloid at $J=2$ signals the change in the tail curvature of $j_{l,J}(E)$ for $E<0$, associated with the discontinuous behavior shown in (a). (c) $E_{\min}(J)$ and $E_{T\min}(J)$ split at $E_c(T=0)=-3$ and $J=1$. For $J\geq 2$, there exist intersection surfaces with zero $\chi_J(E)$ in the region limited by $E_{\min}(J)$ and $E_{T\min}(J)$. The spin structures illustrate the stable phases associated with $E_{\min}(J)$.

The isolated critical points of the Morse function $\mathcal{H}(\theta_A,\theta_B)$ [Eq. (11)] occur for $\theta=\theta_c\in\{0,\pi\}^{2N_c}$, i.e., for $\theta_c=(\theta_{A_1},\ldots,\theta_{A_{N_c}},\theta_{B_1},\ldots,\theta_{B_{N_c}})$ with all components $\theta_{A_i(B_i)}$ being either 0 or π. It is easy to show that the multiplicity of the critical points is $\binom{N_c}{n_{\pi A}}\binom{N_c}{n_{\pi B}}$, where $n_{\pi_{A(B)}}$ is the number of $A(B)$ spins with $\theta_c=\pi$. Therefore, the Morse number reads

$$\mu_k(E)=\binom{N_c}{n_{\pi A}}\binom{N_c}{n_{\pi B}}\Big|_{k(n_{\pi A},n_{\pi B};E)}, \tag{30}$$

where the index $k(n_{\pi A},n_{\pi B})$, without energy restriction, is given by Eqs. (B5)–(B7). The computation of the index k and $\mu_k(E)$, including a discussion on some of their interesting features, is presented in Appendix B.

On the other hand, due to the form of the $\mathcal{H}(\theta_A,\theta_B)$, it is useful to split the Hessian into two blocks; the first one, relative to the A sites and the second one to the B sites,

$$\mathcal{H}^{AB}_{ij}=\mathcal{H}^{A}_{kl}+\mathcal{H}^{B}_{mn}, \quad k,l=1,\ldots,N_c, \quad m,n=N_c+1,\ldots,2N_c. \tag{31}$$

For $N_c\gg 1$, the Hessian is diagonal with matrix elements given by (see Appendix B)

$$\mathcal{H}^{A}_{ii}=-\frac{4\cos\theta_{Ai}}{N_c}m_{Bx}, \tag{32}$$

$$\mathcal{H}^{B}_{ii}=-\frac{1}{N_c}[4m_{Ax}\cos\theta_{Bi}+2J(m_{xB}\cos\theta_{Bi}-m_{yB}\sin\theta_{Bi})]. \tag{33}$$

At an isolated critical point defined above, $\mathcal{H}(\theta_A,\theta_B)$ in Eq. (11) reads

$$E(n_{\pi_A},n_{\pi_B},J)=4\left(1-\frac{2n_{\pi_A}}{N_c}\right)\left(1-\frac{2n_{\pi_B}}{N_c}\right)+J\left(1-\frac{2n_{\pi_B}}{N_c}\right)^2, \tag{34}$$

where use of Eq. (2) was made with $m_{A(B)x}=(1-2n_{\pi A(B)}/N_c)$ and $m_{A(B)y}=0$.

We can now proceed to compute numerically the Euler characteristic, in the convenient normalized form $\ln|\chi_J(E)|/2N_c$, and the density of Jacobian's critical points $j_{l,J}(E)$. In fact, we have computed the first quantity in four equivalent ways, as given by Eqs. (9) and (10), and further use of Eqs. (30), (B5)–(B7), and (34). We stress that the referred four ways of computing $\ln|\chi_J(E)|/2N_c$ give the same result within numerical accuracy after subtraction of the leading finite-size term of $\mathcal{O}(\ln 2N_c/2N_c)$. However, the computational effort using the standard definition, i.e., $\ln|\chi_J(E)|$, is quite high, so that the final computation was done using either of the remained approaches for $N_c=10^3$ and $\delta E=0.01$. Moreover, the computation through Eq. (10) is the simplest one since it needs only the use of Eq. (34). On the other hand, in computing $j_{l,J}(E)$ was made use of its definition in Eq. (6), which requires the computation of the determinant of the Hessian whose diagonal matrix elements are given by Eqs. (32) and (33), and the energy around its value in Eq. (34) with uncertainty δE; in fact, ε is irrelevant in the thermodynamic limit [24]. Therefore, in order to obtain accurate results, the computation was performed for $N_c=10^4$ and $\delta E=0.001$.

In Fig. 4(a) we display $\ln|\chi_J(E)|/2N_c$ measured on the surface defined by the intersection of the equipotential surface and $\mathcal{C}_B$. Notice that it exhibits a cusp at $E_c(T\neq 0)\ \forall\ J$. For $J\geq 2$, $\ln|\chi_J(E)|/2N_c$ is discontinuous at $E_{T\min}$ due to intersection surfaces with zero $\chi_J(E)$ for $E_{\min}(J)\leq E<E_{T\min}(J)$. The intersection surfaces and $\ln|\chi_J(E)|/2N_c$ vanish at $E_{\max}=E_{T\max}=4+J$. The divergence of $j_l(E)$ at $E_c(T\neq 0)\ \forall\ J$ is shown in Fig. 4(b), thus satisfying the necessity criterion at a topology-induced PT [4]. The golden hyperboloid at $J=2$ signals the change in the tail curvature of $j_l(E)$ for $E<0$, associated with the $\ln|\chi_J(E)|/2N_c$ discontinuity shown in Fig. 4(a). Moreover, for $0\leq J\leq 2$, we find that $E_{\min}(J)=E_{T\min}(J)=-4+J$ [see Eq. (26)]. However, $E_{T\min}(J)$ splits from $E_{\min}(J)$ at $E_c(T=0)=-3$ and $J=1$, as shown in Fig. 4(c). In fact, for $1<J\leq 2$, $E_{T\min}(J)$ above corresponds to a metastable Ising solution; further, for $J\geq 2$, $E_{T\min}(J)=-\frac{4}{J}$ and in the region limited by $E_{\min}(J)$ and $E_{T\min}(J)$ we have

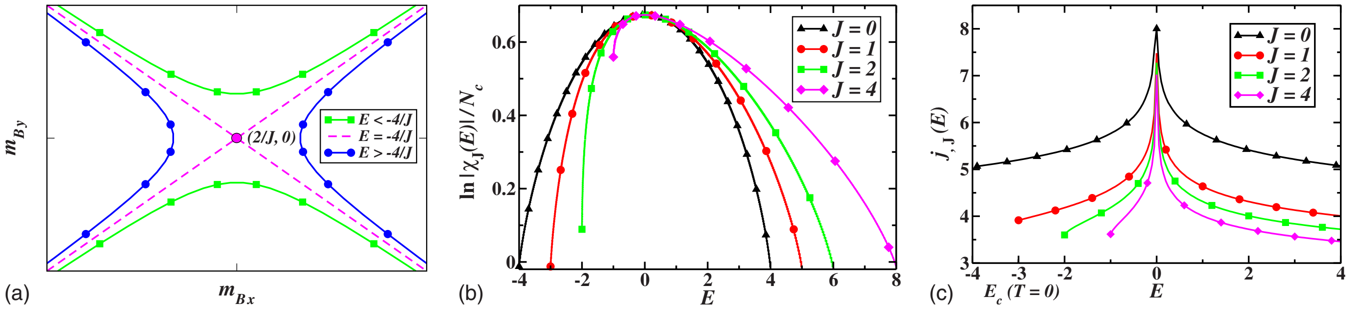

FIG. 5. (Color online) (a) Equipotential curves of the A-frozen frustrated AB_2-XY model: for $E<E_{T\min}(J)=-4/J$, the hyperbola transverse axis is along the x axis (east-west opening hyperbolas); for $E=E_{T\min}(J)=-4/J$ the hyperbolas are degenerate with asymptotes: $m_{By}=\pm(m_{Bx}-2/J)$; and for $E>E_{T\min}(J)$, the hyperbola transverse axis is along the y axis (north-south opening hyperbola). (b) $\ln|\chi_J(E)|/N_c$: no cusplike pattern occurs at $E=0$. (c) Divergence of $j_{l,h}(E)$ at $E=0$ for $J=0$, 1, 2, and 4.

intersection surfaces with zero $\chi_J(E)$. We also emphasize that the topological energies [$E_{T\min}(J)$ and $E_{T\max}(J)$] can be inferred both from $\ln|\chi_J(E)|/2N_c$, $j_{l,J}(E)$, and $\mu_k(E)$ (see Appendix B).

We close our analysis of the frustrated AB_2-XY model by establishing a nontrivial direct connection between the thermodynamics of the system and the topology of its configuration space. In fact, for $0\leq J\leq 1$ ($J>1$), besides the finite-temperature results, we have found that the distinct extremum numerical solutions of the saddle-point consistency equations given above, in a $\mathbb{C}^4$ ($\mathbb{C}^3$) space, give rise to the following energies in the limit $T\to 0$: the piecewise functions $E_{\min}(J)$ and $E_{T\min}(J)$, as defined above [see Fig. 4(c)], where

$$E(T=0,J)=-\lim_{T\to 0}\frac{\partial}{\partial\beta}[\beta F(T;J)]. \tag{35}$$

On the other hand, the MF maximum (and unstable) energy solutions $E_{\max}(J)=E_{T\max}(J)=4+J$ [$E_{T\max}(J)$] is obtained from Fig. 4(a), but not shown in Fig. 4(c), and can be readily derived from Eq. (11). The above results also confirm that the symmetry condition (see Appendix A), which is inferred from the $T=0$ solution, is preserved for all temperatures in the condensed phase.

B. Suppression of the $T\neq 0$ phase transition in the frustrated AB_2-XY model

In Sec. IV we showed that the frustrated AB_2-XY model exhibits topology-induced finite-temperature PT for ∀ J. A remarkable feature is the cusplike behavior displayed by the Euler characteristic at the critical energy $E_c(T\neq 0)=0$. In order to test whether this behavior is a necessity condition for a topology-induced PT, we study this system under a staggered field to keep the magnetization at A sites at a constant value, namely, $m_{Ax}=-1$. Obviously, under this stringent condition, there is no phase transition, and thereby it should manifest in the Euler characteristic.

Under the above-mentioned constraint, the zero-field Hamiltonian [Eq. (11)] reduces to

$$\mathcal{H}(\theta_B)=-4m_{Bx}+J(m_{Bx}^2-m_{By}^2) \tag{36}$$

and the accessible configurations are defined by the disk

$$\mathcal{D}_B=\{(m_{Bx},m_{By}):m_{Bx}^2+m_{By}^2\leq 1\}. \tag{37}$$

Thus, the equipotential submanifolds of the Morse function $\mathcal{H}(\theta_B)$ are obtained by identifying the corresponding conic, given below, under the constraint of $\mathcal{D}_B$ for a given energy E,

$$J\left(m_{Bx}-\frac{2}{J}\right)^2-Jm_{By}^2=E+\frac{4}{J}. \tag{38}$$

We thus get, ∀ J and ∀ E, a rectangular hyperbola, as shown in Fig. 5(a). The properties of the intersection curves between the equipotential hyperbolas and $\mathcal{D}_B$ around $E_{T\min}(J)$ and $E_{\min}(J)$, which attain the same values as in unconstrained case [see Figs. 4(a) and 5(b)], follow the same pattern shown in Fig. 3 under the restriction $m_{Ax}=-1$. In particular, the present analysis makes possible a geometrical interpretation of the metastable solution $E_{T\min}(J)=-4/J$, valid for $J\geq 2$, as explained in the following and illustrated in Fig. 5(a). In fact, for $E<E_{T\min}(J)=-4/J$, the hyperbola transverse axis is align with the x axis (east-west opening hyperbolas); for $E=E_{T\min}(J)=-4/J$ the hyperbolas are degenerate and consist only of its asymptotes: $m_{By}=\pm(m_{Bx}-2/J)$; for $E>E_{T\min}(J)$, the hyperbola transverse axis is align with the y axis (north-south opening hyperbola). Notice that the referred value for $E_{T\min}(J)$ can be found from Eq. (11) using the asymptotic solutions for $\mathbf{m_B}$.

The computed Euler characteristic is illustrated in Fig. 5(b). Since there is no PT, no cusplike pattern occurs at $E=0$ ∀ J and thus suggests that the mentioned pattern is indeed a necessary condition for the occurrence of a topology-induced PT. Nevertheless, even in the absence of a PT the density of Jacobian's critical points is divergent at $E=0$, as shown in Fig. 5(c).

C. AB_2-XY model in a field

We now turn to the case of the AB_2-XY model in a magnetic field along the x direction ($h\neq 0, J=0$). In this case, the appropriate physical symmetry condition implies $\mathbf{m_{B_1}}+\mathbf{m_{B_2}}\equiv 2\mathbf{m_B}$, also under the constraint of zero transversal magnetization (see Appendix A). Thus, $\mathcal{H}(\theta_A,\theta_B)$ reads

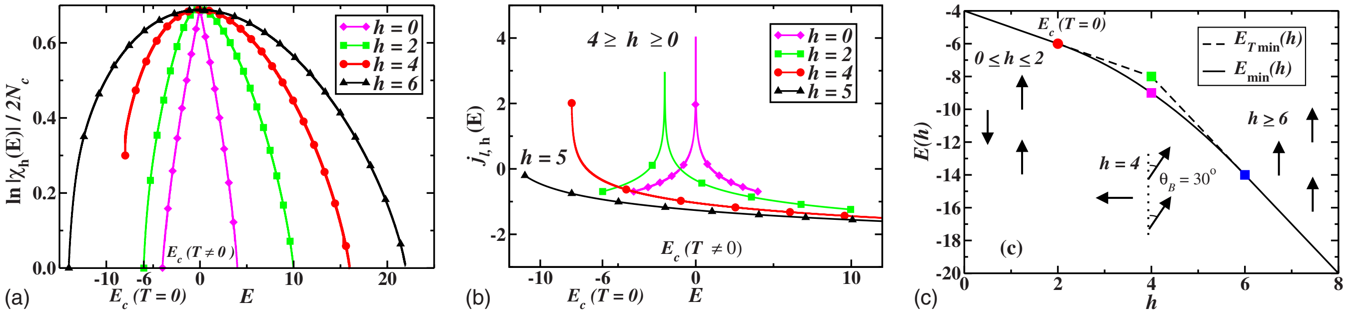

FIG. 6. (Color online) AB_2-XY model in a field. (a) $\ln|\chi_h(E)|/2N_c$: cusplike pattern (discontinuity) occurs only at $h=0$ ($h=4$). (b) Divergence of $j_{l,h}(E)$ at $E_c(T\neq 0)-h^2/2$ for $4\geq h\geq 0$; the PT occurs at $E_c(T\neq 0)=0$ and $h=0$. The divergence is suppressed for fields higher than the spin saturation field predicted by $E_{T\min}(h)$ at $h=4$. (c) $E_{\min}(h)$ and $E_{T\min}(h)$ split at $E_c(T=0)=-6$ and $h=2$; they join again at $h=6$, where saturation occurs as predicted both by $E_{\min}$ and $E_{T\min}$. The illustration of the stable magnetic phases is associated with $E_{\min}(h)$

$$\mathcal{H}(\theta_A,\theta_B)=4(m_{Ax}m_{Bx}+m_{Ay}m_{By})-h(m_{Ax}+2m_{By}), \tag{39}$$

which is the Morse function in the present case.

Here, we use the same procedure as in the previous case to compute the topological invariants and thermodynamic quantities, including the pertinent energies in the limit $T\to 0$. In order to compute the canonical partition function [Eq. (12)], it is useful to write Eq. (39) as follows:

$$\mathcal{H}(\theta_A,\theta_B)=2(\mathbf{m_A}+\mathbf{m_B})^2-2(\mathbf{m}_\mathbf{A}^2+\mathbf{m}_\mathbf{B}^2)-\mathbf{h}\cdot(\mathbf{m_A}+2\mathbf{m_B}). \tag{40}$$

Using the identities [Eqs. (14) and (15)] in a two-dimensional version, we obtain

$$Z(\beta,N_c)=\left(\frac{N_c}{8\pi\beta}\right)^3\int_{-\infty}^{+\infty}\prod_{i=1}^{3}d\mathbf{z_i}\exp\left[-N_c\left(\sum_{i=1}^{3}\frac{\mathbf{z}_\mathbf{i}^2}{8\beta}-\ln 2\pi I_0\right.\right.$$
$$\left.\left.\times(|i\mathbf{z_1}+\mathbf{z_2}+\beta\mathbf{h}|)-\ln 2\pi I_0(|i\mathbf{z_1}+\mathbf{z_3}+2\beta\mathbf{h}|)\right)\right]. \tag{41}$$

Now, the set of consistency equations from the saddle-point method, in a $\mathbb{C}^6$ space, reads

$$\frac{\mathbf{z_3}}{4\beta}-\frac{I_1}{I_0}(|-\mathbf{z_2}+2\beta\mathbf{h}|)\frac{(-\mathbf{z_2}+2\beta\mathbf{h})}{|-\mathbf{z_2}+2\beta\mathbf{h}|}=0, \tag{42}$$

$$\frac{\mathbf{z_2}}{4\beta}-\frac{I_1}{I_0}(|-\mathbf{z_3}+\beta\mathbf{h}|)\frac{(-\mathbf{z_3}+\beta\mathbf{h})}{|-\mathbf{z_3}+2\beta\mathbf{h}|}=0, \tag{43}$$

and

$$\mathbf{z_1}=\mathbf{z_2}+\mathbf{z_3}. \tag{44}$$

Here, the $T\neq 0$ PT occurs only for $h=0$ with $E_c=0$ and $M(T)$ given in Fig. 2 for $J=0$.

The accessible configurations are now the four-dimensional region,

$$\mathcal{C}_h=\{(\mathbf{m_A},\mathbf{m_B}):\mathbf{m}_\mathbf{A}^2\leq 1,\mathbf{m}_\mathbf{B}^2\leq 1\}. \tag{45}$$

However, by using the condition of zero transversal magnetization, i.e., $m_{Ay}=2m_{By}$, we can restrict the analysis of the equipotential surfaces to a tree-dimensional space, which, in fact, display E-dependent topological properties similar to those shown in Fig. 3(a). The isolated critical points are the same, and the Morse number, $\mu_k(E)$, is given by Eq. (30), where the index $k(n_{\pi A},n_{\pi B};h)$, without energy restriction, is given by Eqs. (B11) and (B12). Also, for $N_c\gg 1$ the Hessian is diagonal with matrix elements given by

$$\mathcal{H}_{ii}^{A}=(-4m_{Bx}+h)\frac{\cos\,\theta_{Ai}}{N_c}-4m_{By}\frac{\sin\,\theta_{Ai}}{N_c} \tag{46}$$

and

$$\mathcal{H}_{ii}^{B}=(-4m_{Ax}+2h)\frac{\cos\,\theta_{Bi}}{N_c}-4m_{Ay}\frac{\sin\,\theta_{Bi}}{N_c}. \tag{47}$$

At a given critical point, $\mathcal{H}(\theta_A,\theta_B)$ in Eq. (39) reads

$$E(n_{\pi_A},n_{\pi_B},h)=4\left(1-\frac{2n_{\pi_A}}{N_c}\right)\left(1-\frac{2n_{\pi_B}}{N_c}\right)$$
$$-h\left[\left(1-\frac{2n_{\pi_B}}{N_c}\right)+2\left(1-\frac{2n_{\pi A}}{2N_c}\right)\right]. \tag{48}$$

In analogy with the previous case, we now compute the topological invariants numerically as a function of the energy level E and a fixed magnetic field h using the methods discussed in Sec. II.

In Figs. 6(a) and 6(b) we display $\ln|\chi_h(E)|/2N_c$ and $j_l(E)$ for distinct values of h, respectively. A symmetrical cusplike pattern [see Fig. 6(a)] and a divergence at $E_c(T\neq 0)=0$ [see Fig. 6(b)] occur only for $h=0$, in agreement with the previous case for $J=0$. Nevertheless, for $4\geq h>0$, $j_l(E)$ is singular at energies $E_c(T\neq 0)-h^2/2$, not associated with finite-temperature PT. In addition, a discontinuity in $\ln|\chi_h(E)|/2N_c$ is observed only for $h=4$, the point at which $m_{Ax}=0$; further, at this point, a metastable Ising spin-flip first-order PT is predicted by $E_{T\min}(h)=-4-h=-h^2/2=-8$, thus leading to zero spin degeneracy and suppression of the divergency of $j_l(E)$ for $h>4$; notice that while the previous expression for $E_{T\min}(h)$ holds for $0\leq h\leq 4$, for $h\geq 4$ we find $E_{T\min}(h)=4-3h$ [see Figs. 6(b) and 6(c)]. Moreover, as in the previous

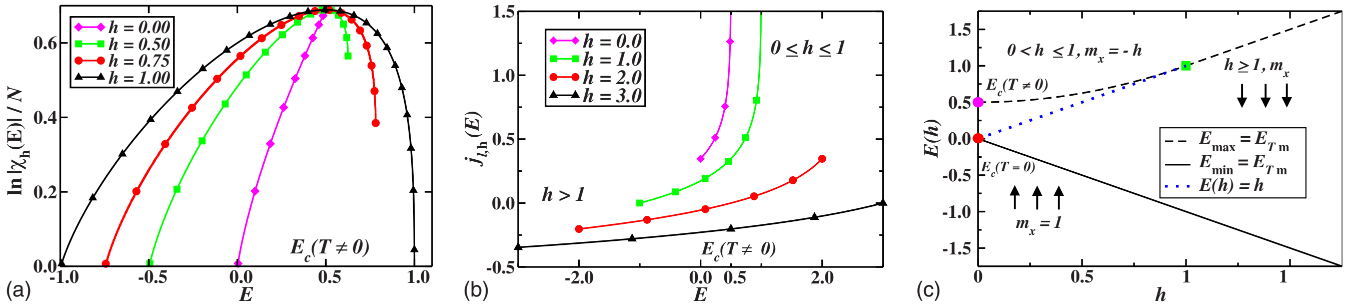

FIG. 7. (Color online) Standard infinite-range *XY* model in a field. (a) $\ln|\chi_h(E)|/N$: cusplike pattern (discontinuity) at (for) $h=0$ $(0 \leq h < 1)$. (b) Divergence of $j_{l,h}(E)$ for $0 \geq h \geq 1$; the PT occurs at $E_c(T \neq 0)=1/2$ and $h=0$. The divergence is suppressed for fields beyond the spin saturation field predicted by $E_{T\max}$ at $h=1$. (c) h-dependent energies and magnetization.

case, the topological energies [$E_{T\min}(h)$ and $E_{T\max}(h)=4+3h$] can be inferred both from $\ln|\chi_h(E)|/2N_c$, $j_{l,h}(E)$, and $\mu_k(E)$ (see Appendix B), as well as from Eq. (39).

In Fig. 6(c), we also show the stable spin configurations at $T=0$. In fact, for $0 \leq h \leq 2$ the system displays the same ferrimagnetic phase as in the frustrated case, while for $h \geq 6$, the system is fully polarized; in both cases $E_{\min}(h) = E_{T\min}(h)$. For $2 \leq h \leq 6$, $E_{\min}(h)=-h^2/4-5$ and, at $h=2$, an interesting continuous spin-flip PT occurs: by increasing h the *A* spins rotate, seeking alignment with the field, while the *B* spins rotate to cancel the unit cell transversal magnetization. In fact, the *B* spins rotate in the opposite direction up to $\theta=30°$ at $h=4$ and then rotate back for higher fields; the net result is a unit cell magnetization increasing linearly with h up to saturation at $h=6$ [18].

D. Standard infinite-range *XY* model revisited

Finally, we use our approach to revisit the standard infinite-range *XY* model with ferromagnetic interactions [4–6,25] in the presence of a magnetic field. The model is a system of N plane rotators described by angular variables $\theta = (\theta_1, \ldots, \theta_N)$ and Hamiltonian (here we do not consider kinetic energy effects) given below,

$$H(\theta) = \frac{1}{2N}\sum_{i,j=1}^{N}[1-\cos(\theta_i-\theta_j)] - h\sum_{i=1}^{N}\cos\,\theta_i. \tag{49}$$

The free energy per particle reads [25]

$$F(z;T,h) = \frac{1}{2} + \frac{1}{\beta}\left(\frac{z^2}{2\beta} - \ln[2\pi I_0(z+\beta h)]\right), \tag{50}$$

where z is the solution of the saddle-point self-consistency equation,

$$\frac{z}{\beta} = \frac{I_1}{I_0}(z+\beta h) = M(z;T,h), \tag{51}$$

with $M(z;T,h)=-\frac{1}{\beta}\frac{\partial F(z;\beta,h)}{\partial h}$. In the limit $h \to 0$, the solution of Eq. (51) is $z=0$ for $\beta < \beta_c = 2$, corresponding to a vanishing magnetization, and $z \neq 0$ for $\beta > \beta_c$. Therefore, since the energy, $E(z;T,h) = -\frac{\partial}{\partial\beta}[\beta F(z;T,h)]$, is given by

$$E(z;T,h) = \tfrac{1}{2}[1-M(z;T,h)^2] - hM(z;T,h), \tag{52}$$

the $T \neq 0$ PT occurs for $E_c=0.5$ and $h=0$.

The critical points of this model are $\theta=\theta_c=\{0,\pi\}^N$. At a given critical point and in the limit $N \gg 1$, the Hessian is diagonal, with matrix elements given by [5,6]

$$\mathcal{H}_{ii}(\theta_c) = \left[\left(1-\frac{2n_\pi}{N}\right)+h\right]\cos\,\theta_i. \tag{53}$$

In zero field, the Euler characteristic (density of Jacobian's critical points) displays discontinuous (divergent) behavior at the critical energy $E_c=0.5$, thereby confirming the topological origin of the finite-temperature PT exhibits by this model [4–6]. The relation between the PT exhibited by this model and the topology of its configuration space is also verified qualitatively considering the sequence of topological transformations undergone by M_E until $E=E_c(T \neq 0)=0.5$ [6].

Here, we are primarily concerned with the field dependence of the above-mentioned topological features and their connection with the thermodynamics of the model. To this aim, we compute numerically $\ln|\chi_h(E)|/N$ and $j_{l,h}(E)$, as shown in Figs. 7(a) and 7(b). From Eq. (52) and Fig. 7(a), we find $E_{\max}(h)=E_{T\max}(h)=1/2+h^2/2$ for $0 \leq h < 1$ and h for $h \geq 1$. As shown in Figs. 7(a) and 7(b), $\ln|\chi_h(E)|/N$ is discontinuous for $0 \leq h < 1$, while $j_{l,h}(E)$ is singular at $E_{T\max}(h) = E_c(T \neq 0)+h^2/2$ for $0 \leq h \leq 1$, with the finite-temperature PT at $E_c(T \neq 0)=1/2$ and $h=0$. In addition, as shown in Fig. 7(a), we also notice that, similarly to the microcanonical configurational entropy [26], there is no positive lower bound for the slope of the Euler characteristic in the presence of a field. In Fig. 7(c), we display the pertinent energies in the limit $T \to 0$: $E_{\min}(h)=E_{T\min}(h)=-h$. First, we note that $E_c(T = 0)=\lim_{h\to 0} E_{\min}=0$ and $M=1$. Further, the two $E_{T\max}(h)$ metastable solutions [25] correspond to $M=-h$ and $M=-1$. Therefore, for $h>1$, $E_{T\max}(h)$ exhibits a nondegenerate state, thus causing the suppression of the singular behavior of $j_l(E)$.

Lastly, in the present model we can provide both a quantitative analysis and a qualitative illustration of the direct connection between thermodynamics and the topology of configuration space. In fact, in the limit $T \to 0$, we find two metastable solutions of Eq. (51) for $h<1$, associated with the metastable solutions for $E_{T\max}(h)$ referred above [see Fig. 8(a) for $h=0.5$ and $T=0.01$ and Fig. 7(c)]. For $h=1$, the metastable solutions coincide [see Fig. 8(b) for $h=1$ and $T = 0.01$ and Fig. 7(c)] beyond which the suppression of the discontinuity (divergence) of $\ln|\chi_h(E)|/N$ [$j_l(E)$] takes place.

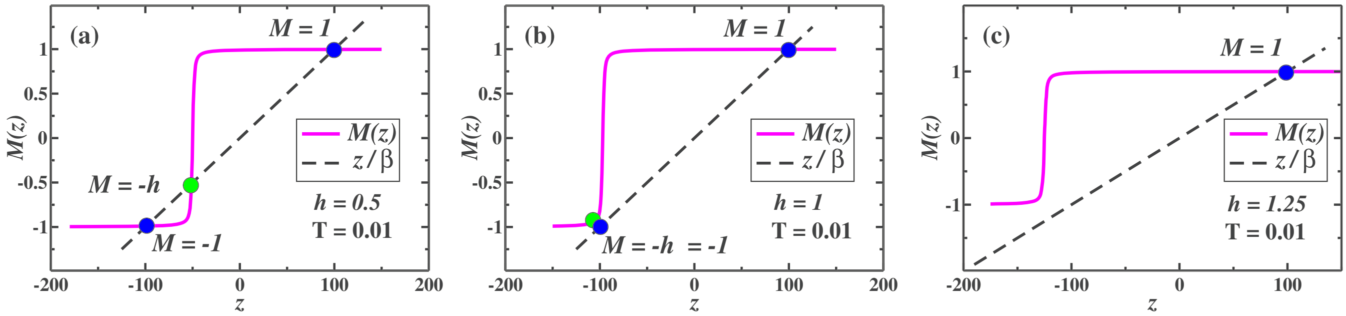

FIG. 8. (Color online) Magnetization of the standard infinite-range XY model at $T=0.01$ (only $h>0$ is illustrated): (a) stable ($M=1$) and metastable ($M=-1$ and $M=-h$) solutions for $h<1$, corresponding to the solutions $E(h)=h$ and $E_{T\max}(h)$ [see Fig. 7(c)]. (b) The two metastable solutions meet at $h=1$. (c) For $h>1$, only the stable solution $M=1$ remains.

For $h>1$, we find that only the minimum solution $M=1$ remains [see Fig. 8(c) for $h=1.25$ and $T=0.01$ and Fig. 7(c)]. However, for $h>1$ and at zero temperature, Eq. (52) also allows for a thermodynamically unstable solution, i.e., $M=-1$, corresponding to $E_{\max}(h>1)=E_{T\max}(h>1)=h$.

IV. CONCLUSIONS

In conclusion, we have presented a quite complete topological characterization of the phase transitions occurring in two infinite-range XY models exhibiting noncollinear spin structures on the AB_2 chain and complemented the analysis of the phase transition displayed by the standard infinite-range XY model. We have computed the Morse number and the Euler characteristic, as well as other topological invariants associated with the model systems, which are found to behave similarly as function of the energy level in the context of Morse theory. For example, the Euler characteristic and other invariants as well have their maximum (or divergence) at the critical energy of the finite-temperature PT. Moreover, we have used an efficient alternative method to compute the Euler characteristic, which proves more feasible. In addition, we have introduced the minimum (maximum) topological energy, $E_{T\min}$ ($E_{T\max}$), below (above) which the topological invariants are zero (or display no variation), which helped us to clarify several properties of the phase transitions, both at zero and finite temperatures. In fact, we showed that $E_{T\min}$ splits from the MF minimum energy curve, $E_{\min}$, at the critical point of the zero-temperature phase transitions. This feature is associated with the noncollinear nature of the spin structure of the frustrated- and field-induced phases. Further, our computation of the density of Jacobian's critical points has confirmed the topological origin of the finite-temperature phase transition for the frustrated AB_2-XY model $\forall$ J and for the AB_2-XY model in zero field. In addition, we have established a nontrivial direct connection between the thermodynamics of the studied models, which have been solved exactly under the saddle-point approach, and the topology of its configuration space. In fact, all the zero-temperature stable and metastable pertinent energies, included the topological ones, are extremum solutions of the saddle-point self-consistent equations in the limit $T\to 0$. This connection has also allowed us to identify the nondegeneracy condition under which the divergence of the density of Jacobian's critical points is suppressed. Finally, our findings and those available in the literature [1–7,24–26] suggest that the cusplike pattern exhibits *both* by the Euler characteristic and the topological contribution for the entropy at the critical energy [3], *put together* with the divergence of density of Jacobian's critical points, and emerge as necessary and *sufficient* conditions for the occurrence of a finite-temperature topology-induced phase transition. The general character of this proposal must be subject to further scrutiny, on a rigorous basis [1,3], and tested on a wider variety of systems, including those with short-range interaction. In summary, our reported findings may shed light on the quest for a proper understanding of the topological properties associated with a phase transition.

ACKNOWLEDGMENTS

We acknowledge fruitful discussions with R. R. Montenegro-Filho, M. Kastner, E. S. G. Leandro, E. J. Pessoa, and F. Parísio. This work was supported by CNPq, FACEPE, Finep, and CAPES (Brazilian agencies).

APPENDIX A: SYMMETRY PROPERTIES OF THE AB_2-XY MODEL

In this appendix we shall examine the symmetry properties of the AB_2-XY model. The results will allow us to simplify the analysis of their topological properties. In particular, these features will turn the computation of the topological invariants and thermodynamic behavior more feasible.

1. Topology of configuration space of the frustrated AB_2-XY model

Here, our goal is to compute the Euler characteristic of the frustrated AB_2-XY model in a general framework, in such a way that the symmetry properties of the model are unveiled.

Inserting the magnetization [Eq. (2)] in Hamiltonian (1) in zero field, we find

$$\mathcal{H} = z_{AB}\mathbf{m}_{\mathbf{A}}\cdot(\mathbf{m}_{\mathbf{B}_1}+\mathbf{m}_{\mathbf{B}_2}) + z_B J\mathbf{m}_{\mathbf{B}_1}\cdot\mathbf{m}_{\mathbf{B}_2}. \tag{A1}$$

The critical points of the Morse function defined by Eq. (A1) are thus found from the equations below,

$$\frac{\partial\mathcal{H}(\theta_A,\theta_{B_1},\theta_{B_2})}{\partial\theta_{\alpha i}}=0,\quad i=1,\ldots,N_c,\quad \alpha=A,B_1,B_2. \tag{A2}$$

For the A spins we thus find

$$\frac{\partial\mathcal{H}(\theta_A,\theta_{B_1},\theta_{B_2})}{\partial\theta_{Ai}}=\frac{z_{AB}}{N_c}[-\sin\,\theta_{A_i}(m_{B_1x}+m_{B_2x}) + \cos_{\theta_{A_i}}(m_{B_1y}+m_{B_2y})]=0, \tag{A3}$$

while for the $B_{1(2)}$ spins we have

$$\frac{\partial\mathcal{H}(\theta_A,\theta_{B_1},\theta_{B_2})}{\partial\theta_{B_{1(2)i}}}=\frac{z_{AB}}{N_c}[-\sin\,\theta_{B_{1(2)i}}m_{Ax}+\cos\,\theta_{B_{1(2)i}}m_{Ay}] + \frac{z_B}{N_c}[-\sin\,\theta_{B_{1(2)i}}m_{B_{2(1)}x} + \cos\,\theta_{B_{1(2)i}}m_{B_{2(1)}y}]=0. \tag{A4}$$

From Eq. (A3), the solutions are $\theta_{Ai_c}\in\{0,\pi\}^{N_c}$ if $m_{B_1y}=-m_{B_2y}$ and $\theta_{Ai_c}\in\{\pi/2,3\pi/2\}^{N_c}$ if $m_{B_1x}=-m_{B_2x}$. On the other hand, from Eq. (A4) the solutions are $\theta_{B_{1(2)ic}}\in\{0,\pi\}^{N_c}$ if $\theta_{Ai_c}\in\{0,\pi\}^{N_c}$ and $\theta_{B_{1(2)i}}\in\{\pi/2,3\pi/2\}^{N_c}$ if $\theta_{Ai_c}\in\{\pi/2,3\pi/2\}^{N_c}$. Therefore, we have two classes of isolated critical points $\theta_c=(\{\theta_{A_{ic}}\},\{\theta_{B_{1ic}}\},\{\theta_{B_{2ic}}\})$ defined by $\theta_c\in\{0,\pi\}^{3N_c}$ and $\theta_c\in\{\pi/2,3\pi/2\}^{3N_c}$. In fact, summing up either Eq. (A3) or (A4) over $\theta_{A_{ic}}$, $\theta_{B_{1ic}}$, and $\theta_{B_{2ic}}$, we find

$$-m_{Ax}(m_{B_1y}+m_{B_2y})+m_{Ay}(m_{B_1x}+m_{B_2x})=0. \tag{A5}$$

The two classes of critical points are thus equivalent, differ only by a rotation, and correspond to the constraint of zero transversal magnetization with respect to the symmetry breaking magnetization direction. To achieve that, the B_1 and B_2 spins cancel their frustration-induced transversal magnetization, while the A spins have no transversal component.

The Morse number thus reads

$$\mu_k(E)=\binom{N_c}{n_{\pi A}}\binom{N_c}{n_{\pi B_1}}\binom{N_c}{n_{\pi B_2}}\Bigg|_{k(n_{\pi A},n_{\pi B_{1(2)}};E)}+\binom{N_c}{n_{(3\pi/2)A}} \times\binom{N_c}{n_{(3\pi/2)B_1}}\binom{N_c}{n_{(3\pi/2)B_2}}\Bigg|_{k(n_{(3\pi/2)A},n_{(3\pi/2)B_{1(2)}};E)}, \tag{A6}$$

where $k(n_{\pi A},n_{\pi B_{1(2)}};E)$ and $k(n_{(3\pi/2)A},n_{(3\pi/2)B_{1(2)}};E)$ are the indices of the critical points with energy less than E. Due to the form of the $\mathcal{H}(\theta_A,\theta_{B_1},\theta_{B_2})$, it is useful to split the Hessian into three blocks relative to A, B_1, and B_2 sites,

$$\mathcal{H}_{ij}^{AB_1B_2}=\mathcal{H}_{kl}^{A}+\mathcal{H}_{mn}^{B_1}+\mathcal{H}_{op}^{B_2},$$

$$k,l=1,\ldots,N_c,\quad m,n=N_c+1,\ldots,2N_c,$$

$$o,p=2N_c+1,\ldots,3N_c. \tag{A7}$$

In fact, the Hessian is diagonal with matrix elements given by

$$\mathcal{H}_{ii}^{A}=-\frac{z_{AB}}{N_c}[\cos\,\theta_{A_i}(m_{B_1x}+m_{B_2x})+\sin\,\theta_{A_i}(m_{B_1y}+m_{B_2y})], \tag{A8}$$

$$\mathcal{H}_{ii}^{B_{1(2)}}=-\frac{z_{AB}}{N_c}[\cos\,\theta_{B_{1(2)i}}m_{Ax}+\sin\,\theta_{B_{1(2)i}}m_{Ay}] - \frac{z_B}{N_c}[\cos\,\theta_{B_{1(2)i}}m_{B_{2(1)}x}+\sin\,\theta_{B_{1(2)i}}m_{B_{2(1)}y}]. \tag{A9}$$

At an isolated critical point, we can use the above results to find the energy level $\mathcal{H}(\theta_A,\theta_{B_1},\theta_{B_2})$ in Eq. (A1),

$$E(n_{\pi(3\pi/2)_{A,B_1,B_2}},J)=z_{AB}\left(1-\frac{2n_{\pi(3\pi/2)_A}}{N_c}\right)\left[\left(1-\frac{2n_{\pi(3\pi/2)_{B_1}}}{N_c}\right)+\left(1-\frac{2n_{\pi(3\pi/2)_{B_2}}}{N_c}\right)\right]+z_BJ \times\left(1-\frac{2n_{\pi(3\pi/2)_{B_1}}}{N_c}\right)\left(1-\frac{2n_{\pi(3\pi/2)_{B_2}}}{N_c}\right). \tag{A10}$$

We can now compute numerically the Euler characteristic as a function of the energy level, as shown in Fig. 9 for $J=2$. We have performed this task using two distinct approaches. In the first one, we consider the two equivalent class solutions described above, without no symmetry breaking. In the second one, we choose the magnetization direction along the x axis, so that only the first class of critical points is considered, i.e., $\theta_c\in\{0,\pi\}^{3N_c}$, with $m_{B_1y}\equiv-m_{B_2y}$ and $m_{B_1x}=m_{B_2x}$.

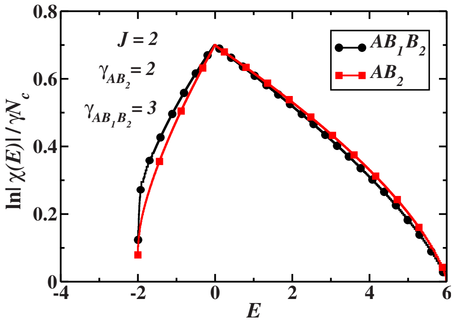

FIG. 9. (Color online) Comparison between computed Euler characteristic with (AB_2) and without (AB_1B_2) symmetry breaking. We used $N_{c;AB_2}=(3/2)N_{c;AB_1B_2}=300$ (see text).

In Fig. 9 we compare the computed Euler characteristic using the two above-mentioned approaches using Eqs. (9) and (10). In order to make the total number of critical points equivalent for $N_c\gg1$ in the two approaches, we make $N_{c;AB_2}=(3/2)N_{c;AB_1B_2}=300$ with point interval $\delta E=0.01$. With this normalization, the results are quite compatible, as shown in Fig. 9, resulting in the same values for $E_{T^{\min}}$ and $E_{T^{\max}}$ and cusplike pattern at $E_c(T\neq 0)=0$. Therefore, in this work we shall use approach one to study the AB_2-XY model in detail.

2. Field effect on topology of configuration space

Here, we analyze the symmetry properties of the nonfrustraded AB_2-XY model in the presence of a field along the x direction. Under these conditions and using the definition of magnetization [Eq. (2)], Hamiltonian (1) reads

$$\mathcal{H} = z_{AB}\mathbf{m_A}\cdot(\mathbf{m_{B_1}}+\mathbf{m_{B_2}}) - \mathbf{h}\cdot(\mathbf{m_A}+\mathbf{m_{B_1}}+\mathbf{m_{B_2}}). \tag{A11}$$

In this case, the critical points of the Morse function [Eq. (A11)] are found from Eq. (A2),

$$\frac{\partial\mathcal{H}(\theta_A,\theta_{B_1},\theta_{B_2})}{\partial\theta_{\alpha i}} = 0, \quad i=1,\ldots,N_c, \quad \alpha=A,B_1,B_2. \tag{A12}$$

We thus find for the A and $B_{1(2)}$ spins, respectively,

$$\frac{\partial\mathcal{H}(\theta_A,\theta_{B_1},\theta_{B_2})}{\partial\theta_{Ai}} = \frac{1}{N_c}\{-\sin\,\theta_{A_i}[z_{AB}(m_{B_1x}+m_{B_2x})-h] + \cos_{\theta_{A_i}} z_{AB}(m_{B_1y}+m_{B_2y})\} = 0, \tag{A13}$$

$$\frac{\partial\mathcal{H}(\theta_A,\theta_{B_1},\theta_{B_2})}{\partial\theta_{B_{1(2)i}}} = \frac{1}{N_c}[-\sin\,\theta_{B_{1(2)i}}(z_{AB}m_{Ax}-h) + \cos\,\theta_{B_{1(2)i}}z_{AB}m_{Ay}] = 0. \tag{A14}$$

Finally, summing up Eq. (A14) over $\theta_{\alpha i}$, $\alpha=A,B_1$, and B_2, we obtain

$$h(m_{Ay}+m_{B_1y}+m_{B_2y}) = 0. \tag{A15}$$

Therefore, the constraint of zero transversal magnetization in a field involves the components of A and $B_{1(2)}$ spins. Notice also that by taking $\mathbf{m_B}=(1/2)(\mathbf{m_{B_1}}+\mathbf{m_{B_2}})$, which is in fact a symmetry property, we can map Eqs. (46) and (47) onto the Hessian computed from Eqs. (A13) and (A14), respectively.

3. Thermodynamics of the frustrated AB_2-XY model

In this section we are interested in the thermodynamics of the frustrated AB_2-XY model, which can be exactly derived in the saddle-point framework. Therefore, using the identities

$$\mathbf{S}_{A_i}\cdot(\mathbf{S}_{B_{1j}}+\mathbf{S}_{B_{2j}}) = \tfrac{1}{2}[(\mathbf{S}_{A_i}+\mathbf{S}_{B_{1i}}+\mathbf{S}_{B_{2j}})^2 - \mathbf{S}_{A_i}^2 - (\mathbf{S}_{B_{1i}}+\mathbf{S}_{B_{2j}})^2], \tag{A16}$$

$$\mathbf{S}_{B_{1i}}\cdot\mathbf{S}_{B_{2j}} = \tfrac{1}{2}[(\mathbf{S}_{B_{1i}}+\mathbf{S}_{B_{2j}})^2 - \mathbf{S}_{B_{1i}}^2 + \mathbf{S}_{B_{2j}}^2) \tag{A17}$$

and the definition of magnetization [Eq. (2)], Hamiltonian (1) can thus be written in a quadratic form,

$$H = \frac{N_c}{2}[z_{AB}(\mathbf{m_A}+\mathbf{m_{B_1}}+\mathbf{m_{B_2}})^2 - z_A\mathbf{m_A^2} + (z_BJ-z_{AB})(\mathbf{m_{B_1}}+\mathbf{m_{B_2}})^2 - z_BJ(\mathbf{m_{B_1}^2}+\mathbf{m_{B_2}^2})]. \tag{A18}$$

Now, in order to compute the partition function

$$\mathcal{Z}(\beta,N_c) = \int_0^{2\pi}\prod_{i=1}^{N_c} d\theta_{A_i}d\theta_{B_{1i}}d\theta_{B_{1i}}\exp(-\beta H), \tag{A19}$$

we use the identity

$$\exp(-c_i\mathbf{y}_i^2) = \frac{1}{\pi}\int_{-\infty}^{+\infty}\exp(-\mathbf{x}_i^2 + 2i\sqrt{c_i}\mathbf{x}_i\cdot\mathbf{y}_i)d\mathbf{x}_i. \tag{A20}$$

We thus find

$$\mathcal{Z}(\beta,N_c) = \left(\frac{N_c}{2\beta\pi^2}\right)^{5/2}\int_0^{2\pi}\prod_{i=1}^{N_c} d\theta_{A_i}d\theta_{B_{1i}}d\theta_{B_{2i}}\int_{-\infty}^{+\infty}\prod_{i=1}^{5} d\mathbf{w}_i\exp N_c\Bigg(-\sum_{i=1}^{5}\frac{w_i^2}{2\beta} + z_{AB}(i\mathbf{w}_1-\mathbf{w}_3)\mathbf{m_A} + [i(\sqrt{z_{AB}}\mathbf{w}_1+\sqrt{z_BJ-z_{AB}}\mathbf{w}_2) - \sqrt{z_BJ}\mathbf{w}_4]\mathbf{m_{B_1}} + [i(\sqrt{z_{AB}}\mathbf{w}_1+\sqrt{z_BJ-z_{AB}}\mathbf{w}_2) - \sqrt{z_BJ}\mathbf{w}_5]\mathbf{m_{B_2}}\Bigg). \tag{A21}$$

Notice that $\mathcal{Z}(\beta,N_c)$ is invariant under the exchange of the magnetization of B sites. Performing the integrals over the angular variables, we have

$$\mathcal{Z}(\beta,N_c) = \left(\frac{N_c}{2\beta\pi^2}\right)^{5/2}\int_{-\infty}^{+\infty}\prod_{i=1}^{5} d\mathbf{w}_i\exp N_c\Bigg(-\sum_{i=1}^{5}\frac{w_i^2}{2\beta} + \ln 2\pi I_0[z_{AB}(i\mathbf{w}_1-\mathbf{w}_3)] + \ln 2\pi I_0\{[i(\sqrt{z_{AB}}\mathbf{w}_1+\sqrt{z_BJ-z_{AB}}\mathbf{w}_2) - \sqrt{z_BJ}\mathbf{w}_4]\} + \ln 2\pi I_0\{[i(\sqrt{z_{AB}}\mathbf{w}_1+\sqrt{z_BJ-z_{AB}}\mathbf{w}_2) - \sqrt{z_BJ}\mathbf{w}_5]\}\Bigg), \tag{A22}$$

where I_0 is the zero-order modified Bessel function. With the aim to compute the free energy given by

$$F = -\lim_{N_c \to \infty} \frac{1}{\beta N_c} \ln Z(\beta, N_c), \tag{A23}$$

using the saddle-point method, we search for the stationary points of

$$\begin{aligned} f = -\sum_{i=1}^{5} \frac{w_i^2}{2\beta} &+ \ln 2\pi I_0[z_{AB}(i\mathbf{w}_1 - \mathbf{w}_3)] \\ &+ \ln 2\pi I_0\{[i(\sqrt{z_{AB}}\mathbf{w}_1 + \sqrt{z_B J - z_{AB}}\mathbf{w}_2) - \sqrt{z_B J}\mathbf{w}_4]\} \\ &+ \ln 2\pi I_0\{[i(\sqrt{z_{AB}}\mathbf{w}_1 + \sqrt{z_B J - z_{AB}}\mathbf{w}_2) - \sqrt{z_B J}\mathbf{w}_5]\}. \end{aligned} \tag{A24}$$

Thereby, we find a self-consistent system in a $\mathbb{C}^{10}$ space, corresponding to $\partial f / \partial \mathbf{w}_i = 0$, $i = 1, \ldots, 5$. We emphasize that the forms of the self-consistent equations associated to $\mathbf{m}_{\mathbf{B}_1}$ and $\mathbf{m}_{\mathbf{B}_1}$ are identical except for the correspondence $\mathbf{w}_4 \leftrightarrow \mathbf{w}_5$. In fact, notwithstanding the numerical difficult to obtain solutions of this nonlinear system, we have succeeded in getting some solutions for particular values of frustration J and temperature T and verified that the constraint condition of zero transversal magnetization obtains and that $\mathbf{w}_4 = \mathbf{w}_5$, which implies $\mathbf{m}_{\mathbf{B}_1} = \mathbf{m}_{\mathbf{B}_2}$. We also remark that similar conclusions also obtain for the nonfrustrated AB_2-XY model in the presence of a field.

APPENDIX B: ADDITIONAL TOPOLOGICAL INVARIANTS

Here, we would like to discuss some details associated with the indices of the critical points, which we have used in Secs. II and III to compute the Euler characteristic and the density of Jacobian's critical points, both in the limit $N_c \gg 1$. We also compute other topological invariants that corroborate general features found in previous ones.

1. Frustration-dependent topological invariants

Now, we want to determine the number k of negative eigenvalues of the Hessian matrix of the Hamiltonian $\mathcal{H}(\theta_A, \theta_B)$ [Eq. (11)]. We split the Hessian in two blocks, H^A and H^B. The diagonal elements of the Hessian are

$$\mathcal{H}_{ii}^{A} = -\frac{4\cos\theta_{Ai}}{N_c} m_{Bx}, \tag{B1}$$

$$\begin{aligned} \mathcal{H}_{ii}^{B} = -\frac{1}{N_c}[4m_{Ax}\cos\theta_{Bi} + 2J(m_{xB}\cos\theta_{Bi} - m_{yB}\sin\theta_{Bi})] \\ - \frac{2J}{N_c^2}\cos 2\theta_{Bi} \end{aligned} \tag{B2}$$

and the off-diagonal ones are

$$\mathcal{H}_{ij}^{A} = \frac{\partial^2 \mathcal{H}(\theta_A, \theta_B)}{\partial \theta_{Ai}\, \partial \theta_{Bj}} = \frac{\partial^2 \mathcal{H}}{\partial \theta_{Bi}\, \partial \theta_{Aj}} = 0, \quad i,j = 1, \ldots, N_c \tag{B3}$$

and

$$\mathcal{H}_{ij}^{B} = -\frac{2J}{N_c^2}\cos(\theta_{Bi} + \theta_{Bj}). \tag{B4}$$

Note that when $i = j$ in Eq. (B4), the last term in Eq. (B2) is equal to Eq. (B4).

At a given critical point and for $N_c \gg 1$, the index k of the critical point can be approximated by the number of negative elements of $\mathcal{O}(1/N_c)$ in Eqs. (B1) and (B2). In fact, since the Hessian elements of $\mathcal{O}(1/N_c^2)$ form a matrix of rank one, the contribution of these terms to the signal of the eigenvalues of the Hessian is irrelevant [5,6]. Therefore, k is given by the number of negative elements of $\mathcal{O}(1/N_c)$ in Eqs. (B1) and (B2). Since the angles θ_{Ai} and θ_{Bi} are either 0 or π, the index reads

$$\text{index } k(n_{\pi A}, n_{\pi B}) = \text{index}_A(n_{\pi A}, n_{\pi B}) + \text{index}_B(n_{\pi A}, n_{\pi B}), \tag{B5}$$

with

$$\text{index}_A = \begin{cases} n_{\pi A} & \text{if } n_{\pi B} > \dfrac{N_c}{2} \\ N_c - n_{\pi A} & \text{if } n_{\pi B} < \dfrac{N_c}{2} \\ 0 & \text{if } n_{\pi B} = \dfrac{N_c}{2}, \end{cases} \tag{B6}$$

where the last result in Eq. (B6) requires N_c even, and

$$\text{index}_B = \begin{cases} n_{\pi B} & \text{if } 2\left(1 - \dfrac{2n_{\pi_A}}{N_c}\right) + J\left(1 - \dfrac{2n_{\pi_B}}{N_c}\right) > 0 \\ N_c - n_{\pi B} & \text{if } 2\left(1 - \dfrac{2n_{\pi_A}}{N_c}\right) + J\left(1 - \dfrac{2n_{\pi_B}}{N_c}\right) < 0 \\ 0 & \text{if } 2\left(1 - \dfrac{2n_{\pi_A}}{N_c}\right) + J\left(1 - \dfrac{2n_{\pi_B}}{N_c}\right) = 0. \end{cases} \tag{B7}$$

Now using Eqs. (30), (34), and (B5)–(B7), we can compute numerically $\ln \mu_k(E)/2N_c$ versus k. From these diagrams, we can also determine $E_{T\min}(J)$ and $E_{T\max}(J)$. In fact, for $E < E_{T\min}(J)$, there are no critical points. For $E_{T\min}(J) \leq E < E_{T\max}$ the diagram is being filled and for $E = E_c(T \neq 0) = 0$ $\forall$ J, $\ln \mu_k(E)/2N_c$ reaches its maximum value at $k = N_c$. For $E \geq E_{T\max}(J)$, the diagram is fulfilled. In Figs. 10(a) and 10(b) we illustrate these features for $J = 2$. For $E < E_{T\min}(J=2) = -2$, there are no critical points. In Fig. 10(a), we show the diagram for $E = E_c(T \neq 0) = 0$, which displays the maximum of $\ln \mu_k(E)/2N_c$ at $k = N_c = 500$. In Fig. 10(b) for $E \geq E_{T\max}(J=2) = 6$, the diagram is fulfilled.

We also remark that if $\text{index}_A = 0$, i.e., $n_{\pi B} = N_c/2$, with N_c even [see Eq. (B6)], we have $\text{index} = N_c/2$ $\forall$ J. This result implies in values of $\ln \mu_k(E)/2N_c$ lying in a vertical disjoint line defined by $k = N_c/2 = 250$, as shown in Fig. 10. Moreover, if $\text{index}_B = 0$, i.e. [see Eq. (B7)],

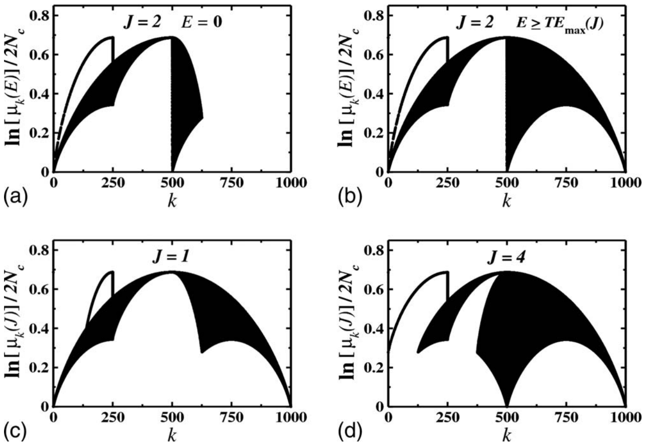

FIG. 10. (a) ln[$\mu_k(E)$]/$2N_c$ for $J=2$ and $E=E_c(T\neq 0)=0$, exhibiting the maximum at $k=N_c=500$; (b) for $E\geq E_{T\max}(J)=6$, the diagram is fulfilled. ln[$\mu_k(J)$]/$2N_c$ for $E\geq E_{T\max}(J)$: for $0\leq J<2$, the filled area of the diagram grows up to $J=2$; for higher values of J, the points at left of the vertical disjoint line ($k=N_c/2=250$) are shifted to the right of this line, as illustrated in (c), (b), and (d) for $J=1$, $J=2$, and $J=4$, respectively. The vertical disjoint lines and curves are explained in the text.

$$2(N_c-2n_{\pi_A})+J(N_c-2n_{\pi_B})=0, \tag{B8}$$

it will prove useful to write $n_{\pi B}=N_c/2\pm\delta_B$ for $n_{\pi B}\geq N_c/2$ or $n_{\pi B}\leq N_c/2$, respectively, where $\delta_B=0,\ldots,N_c/2$, which implies (here we consider N_c even, without loss of generality)

$$\text{index}\ \ k(n_{\pi A},n_{\pi B})=\tfrac{1}{2}(N_c-\delta_B J). \tag{B9}$$

Therefore, since the index $\in\{0,\ldots,2N_c\}$, the above result holds only for $J\in\mathbb{N}$, and Eq. (B8) thus becomes a linear Diophantine equation whose solutions are $n_{\pi A}$ and $n_{\pi B}$. This implies in values of ln $\mu_k(E)/2N_c$ lying in a disjoint curve, $\forall\ J\in\mathbb{N}$, which meets the vertical line referred above at $k=N_c/2=250$, as shown in Fig. 10.

With aim of understanding the influence of the frustration interaction J in the Morse number, we also compute this quantity without energy restrictions, ln $\mu_k(J)/2N_c$, which corresponds to the definition in Eq. (30) for $E\geq E_{T\max}(J)=4+J$. In this regime of energies, for $0\leq J<2$, the filled area of the diagram grows up to $J=2$, the value for which the magnetization vanishes. For higher values of J, the points at left of the vertical disjoint line ($k=N_c/2=250$) are continuously shifted to the right of this line. We illustrate this feature in Figs. 10(c) and 10(d) for $J=1$ and $J=4$, respectively.

We also compute the topological contribution to the entropy per unit cell $\tau(E)$ that, as in [5,6], can be well approximated by

$$\tau(E)=\frac{1}{2N_c}\ln N_{cp}(E), \tag{B10}$$

where $N_{cp}(E)=\sum_{k=1}^{2N_c}\mu_k(E)$ is the total number of critical points of $\mathcal{H}(\theta_A,\theta_B)$ in the manifold M_E. The behavior of $\tau(E)$ is plotted in Fig. 11. For $E<E_{T\min}(J)$ there is no topological contribution to the entropy. For $E\geq E_{T\min}(J)$, the contribution is nonzero and $\tau(E)$ reaches its maximum at $E_c(T\neq 0)=0$ $\forall\ J$ and remains constant for $E\geq E_c=0$; notice also the discontinuity in its slope at $E=0\pm\varepsilon\to 0$. Moreover, for $E\leq E_c=0$, Fig. 11 displays a pattern similar to that exhibited by $\ln|\chi_J(E)|/2N_c$ in Fig. 4(a). Under the constraint $m_{Ax}=-1$, the curves present no cusplike singularity, as shown in Fig. 11(b).

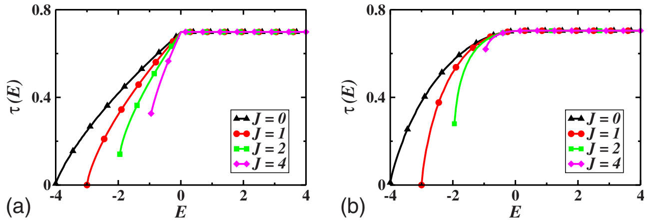

FIG. 11. (Color online) J dependence of $\tau(E)$. (a) The maximum occurs at $E_c(T\neq 0)=0$ $\forall\ J$ and $\tau(E)$ remains at this value for $E\geq E_c=0$; notice the discontinuity in the slope at $E=0\pm\varepsilon\to 0$. (b) Under the constraint $m_{Ax}=-1$, the curves present no cusplike behavior.

2. Field-dependent topological invariants

We now turn to the case of the AB_2-XY model in a magnetic field using similar methods to compute ln $\mu_k(E)/2N_c$, ln $\mu_k(h)/2N_c$, and $\tau(E)$. Using the same procedure of Appendix B 1, the index of the Hessian is given by Eq. (B5) with

$$\text{index}_A=\begin{cases} n_{\pi A} & \text{if}\ \ h>4\left(1-\dfrac{2n_{\pi B}}{N_c}\right)\\ N_c-n_{\pi A} & \text{if}\ \ h<4\left(1-\dfrac{2n_{\pi B}}{N_c}\right)\\ 0 & \text{if}\ \ h=4\left(1-\dfrac{2n_{\pi B}}{N_c}\right)\end{cases} \tag{B11}$$

and

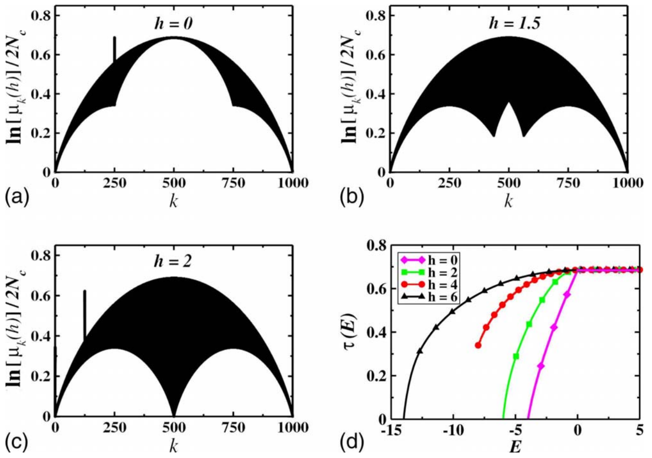

FIG. 12. (Color online) ln[$\mu_k(h)$]/$2N_c$ for $E\geq E_{T\max}(h)$ is displayed in (a)–(c): for $0\leq h<2$, the diagram is being filled and at the critical field value of the $T=0$ PT, $h=2$, the diagram reaches its final form; the vertical disjoint lines are explained in the text. (d) h dependence of $\tau(E)$: the discontinuity in slope of $\tau(E)$ at $E_c(T\neq 0)=0$ shows up only for $h=0$.

$$\text{index}_B = \begin{cases} n_{\pi B} & \text{if } h > 2\left(1 - \dfrac{2n_{\pi B}}{N_c}\right) \\ N_c - n_{\pi B} & \text{if } h < 2\left(1 - \dfrac{2n_{\pi A}}{N_c}\right) \\ 0 & \text{if } h = 2\left(1 - \dfrac{2n_{\pi A}}{N_c}\right). \end{cases} \qquad \text{(B12)}$$

Since ln $\mu_k(E)/2N_c$ has equivalent properties with respect to the frustrated case, here we only show $\ln[\mu_k(h)]/2N_c$, i.e., the Morse number for $E \geq E_{T^{\max}}(h)$. In Figs. 12(a)–12(c) we display $\ln[\mu_k(h)]/2N_c$: for $0 \leq h < 2$, the diagram is being filled and at the critical field value of the $T=0$ PT, $h=2$, the diagram reaches its final form, with two symmetrical arcs around $k=N_c=500$. Therefore, this quantity was very sensitive to the critical field value of the $T=0$ phase transition. Moreover, arguments similar to those used for the frustrated case can explain the occurrence of vertical disjoint lines at $h=0$, 1, 2, and 4.

Finally, the behavior of the topological contribution to the entropy is shown in Fig. 12(d). We stress that the discontinuity in its slope occurs only for $h=0$, in agreement with the results for $\ln|\chi_h(E)|/2N_c$ in Fig. 6(a).

[1] M. Pettini, *Geometry and Topology in Hamiltonian Dynamics and Statistical Mechanics* (Springer, New York, 2007); M. Kastner, Rev. Mod. Phys. **80**, 167 (2008).

[2] L. Caiani, L. Casetti, C. Clementi, and M. Pettini, Phys. Rev. Lett. **79**, 4361 (1997).

[3] R. Franzosi and M. Pettini, Phys. Rev. Lett. **92**, 060601 (2004); R. Franzosi, M. Pettini, and L. Spinelli, Nucl. Phys. B **782**, 189 (2007); R. Franzosi and M. Pettini, *ibid.* **782**, 219 (2007); see also M. Pettini, *Geometry and Topology in Hamiltonian Dynamics and Statistical Mechanics* (Springer, New York, 2007), Chaps. 8 and 9.

[4] M. Kastner, S. Schreiber, and O. Schnetz, Phys. Rev. Lett. **99**, 050601 (2007); M. Kastner and O. Schnetz, *ibid.* **100**, 160601 (2008).

[5] L. Casetti, M. Pettini, and E. G. D. Cohen, Phys. Rev. E **65**, 036112 (2002).;L. Casetti, M. Pettini, and E. G. D. Cohen, J. Stat. Phys. **111**, 1091 (2003).

[6] L. Casetti, E. G. D. Cohen, and M. Pettini, Phys. Rev. Lett. **82**, 4160 (1999).

[7] L. Angelani, L. Casetti, M. Pettini, G. Ruocco, and F. Zamponi, Phys. Rev. E **71**, 036152 (2005).

[8] S. Risau-Gusman, A. C. Ribeiro-Teixeira, and D. A. Stariolo, Phys. Rev. Lett. **95**, 145702 (2005).

[9] See M. Pettini, *Geometry and Topology in Hamiltonian Dynamics and Statistical Mechanics* (Springer, New York, 2007), Chap. 10, p. 345.

[10] P. Grinza and A. Mossa, Phys. Rev. Lett. **92**, 158102 (2004).

[11] L. N. Mazzoni and L. Casetti, Phys. Rev. Lett. **97**, 218104 (2006).

[12] For a recent review, see M. D. Coutinho-Filho, R. R. Montenegro-Filho, E. P. Raposo, C. Vitoriano, and M. H. Oliveira, J. Braz. Chem. Soc. **19**, 232 (2008); R. R. Montenegro-Filho and M. D. Coutinho-Filho, Phys. Rev. B **78**, 014418 (2008).

[13] H. Kikuchi, Y. Fujii, M. Chiba, S. Mitsudo, T. Idehara, T. Tonegawa, K. Okamoto, T. Sakai, T. Kuwai, and H. Ohta, Phys. Rev. Lett. **94**, 227201 (2005); K. C. Rule, A. U. B. Wolter, S. Süllow, D. A. Tennant, A. Brühl, S. Köhler, B. Wolf, M. Lang, and J. Schreuer, *ibid.* **100**, 117202 (2008).

[14] R. R. Montenegro-Filho and M. D. Coutinho-Filho, Physica A **357**, 173 (2005).

[15] Y. V. Korshak, T. V. Medvedeva, A. A. Ovchinnikov, and V. N. Spector, Nature (London) **326**, 370 (1987); H. Nishide, Adv. Mater. **7**, 937 (1995); see also G. Hu, K. He, S. Xie, and A. Saxena, J. Chem. Phys. **129**, 234708 (2008).

[16] G. Parisi, *Statistical Field Theory* (Westview Press, Boulder, CO, 1998), Chap. 3; see also C. J. Thompson, *Classical Equilibrium Statistical Mechanics* (Oxford University Press, Oxford, 1988), Chap. 4; for problems arising in a saddle-point solution for a quantum system, see, e.g., C. A. Macêdo, M. D. Coutinho-Filho, and M. A. de Moura, Phys. Rev. B **25**, 5965 (1982).

[17] Numerical simulation using a single-site mean-field approximation for the ground state of a quantum-rotor model on the frustrated AB_2 chain shown in Fig. 1(a) implies results identical to those derived using Hamiltonian (1) in zero field: A. S. F. Tenório, R. R. Montenegro-Filho, and M. D. Coutinho-Filho Phys. Rev. B **80**, 054409 (2009).

[18] Our zero-temperature MF results using Hamiltonian (1) in the presence of a magnetic field but with $J_2 \equiv J=0$ are also equivalent to those derived in a previous work: C. Vitoriano, M. D. Coutinho-Filho, and E. P. Raposo, J. Phys. A **35**, 9049 (2002).

[19] J. Milnor, *Morse Theory* (Princeton University Press, Princeton, 1963).

[20] V. Guillemin and A. Pollack, *Differential Topology* (Prentice-Hall, Englewood Cliffs, 1974).

[21] It is well known that odd-dimensional compact manifolds have zero Euler characteristic, see, e.g., A. Hatcher, *Algebraic Topology* (Cambridge University Press, Cambridge, 2002).

[22] E. Lieb and D. Mattis, J. Math. Phys. **3**, 749 (1962); G. S. Tian, J. Phys. A **27**, 2305 (1994).

[23] For other values of J and z_{AB}, we can find other metallic means, see, e.g., V. W. de Spinadel, Nonlinear Anal. Theory, Methods Appl. **36**, 721 (1999).

[24] M. Kastner, O. Schnetz, and S. Schreiber, J. Stat. Mech.: Theory Exp. (2008) 04025.

[25] M. Antoni and S. Ruffo, Phys. Rev. E **52**, 2361 (1995).

[26] L. Casetti and M. Kastner, Physica A **384**, 318 (2007).